3D Printed Graphene/Nickel Electrodes for High Areal Capacitance Electrochemical Storage

Guijun Li, Xiaoyong Mo, Wing-Cheung Law and Kang Cheung Chan*

Advanced Manufacturing Technology Research Centre

Department of Industrial and Systems Engineering

Hong Kong Polytechnic University, Hong Kong

*E-mail: kc.chan@polyu.edu.hk

Abstract

Consumer grade supercapacitors as power supply resources require outstanding electrode materials with large conductivity, high durability and retention rates, as well as large capacity. Graphene is a promising functional material as electrical double layer capacitance electrode due to its large surface area, high chemical stability and moderate conductivity. However, the existing graphene synthesis methods, including CVD and chemical exfoliation, are limited at lab scale production. Although laser induced graphene has demonstrated outstanding performance as electrode materials for microsupercapacitor, its difficulty to attach to metallic current collector limits its application as large capacity electrode materials. Herein, laser induced forward transfer of graphene is developed for additive depositing laser induced graphene onto nickel foam as composite electrode. The laser annealing enhanced lattice matching between the extended Basel plane of graphene and Ni(111) prompts its high electrical

conductivity (359,712 S/m), high retention rate (over 98% capacitance retention after 10,000 cycles), large areal specific capacitance (995 mF/cm^2) and power densities (9.39 mW/cm^2). The assembled supercapacitors with these additive printed electrodes can work as USB charger with stable 5 V output voltage, for charging smart phones and other smart devices.

Video Abstract:

https://youtu.be/jehxkRtvmmE

Introduction

Although the development of mobile devices (such as mobile phones, smart watches, wearable sensors, RFID tags and other portable devices) is booming, the technologies of the powering units for such devices are progressing slowly.[1] The long charging duration, up to hours, usually leads to an unsatisfactory user experience. Although power banks can partially solve the slow charging issues by charging the devices during use, these power banks themselves, usually made of batteries, need a rather long charging time.[2] Compared to batteries, supercapacitors are energy storage devices with fast charging features. Instead of utilizing the Faradaic redox reaction, like batteries, supercapacitors make use of the electrical double layer capacitance (EDLC) for storing the energy.[3] The electrostatic Helmholtz double layer at the electrolyte and

electrode interface ensures the fast charging of the supercapacitor. The porous structures of electrode materials are crucial for supercapacitor, and the recent developed novel carbon-based materials have demonstrating outstanding performance as supercapacitor electrode.[4-7]

Laser-induced graphene (LIG) has been intensively studied in regard to its applications in supercapacitor electrodes during the past four years, due to one-step easy processing and roll-to-roll manufacturing compatibility.[8] Although these LIG supercapacitor have demonstrated high performance in micro-supercapacitor applications, their inner resistances increase significantly as larger capacitance devices due to the relatively poor conductivity of semiconducting graphene compared to metals. Common metal current collectors can barely contact the LIG electrode (due to the remaining insulating polyimide beneath the LIG), so only silver paste can be applied to such microsupercapacitors for in-lab demonstration.[9] For optimizing the supercapacitor electrode with low resistance and high volume, composite electrodes with carbon active materials and metal current collectors architectures are usually used.[10] Ultrahigh power density was achieved with onion-like carbon on patterned gold current collectors on silicon wafers.[11] Monolithic carbide-derived carbon supercapacitors have also been fabricated with patterned gold current collectors.[12] Furthermore, nickel also possesses high performance at significantly low cost, and has been intensively studied as current collectors and electrodes for supercapacitor and battery applications.[13-17] For achieving high performance, a fast charging graphene supercapacitor has been fabricated with CVD grown graphene on a nickel substrate.[18]

Laser induced forward transfer (LIFT) is a novel type of 3D printing, enabling high resolution printing of functional materials onto desired locations.[19] Recently, we developed a continuous wave (CW) LIFT method for simultaneous photosynthesis and additive depositing of copper onto various substrates.[20] We also demonstrated the capability of using a 1064 nm CW laser for fabricating graphene Janus wetting membranes for solar-driven desalination.[21] By artificially controlling the superhydrophilic arrays, we fabricated wearable fluid capture devices for in-situ measuring the glucose levels within sweat.[22] In addition, we have undertaken an in-depth study of the photo reduction mechanism of graphene oxides and other oxides under laser scribing.[23, 24] Based on the above findings, herein we further develop a novel graphene deposition method, combining simultaneously laser synthesis as well as LIFT printing, for the additive manufacturing of scalable graphene/nickel based supercapacitor electrodes. The post laser treatment significantly enhanced the lattice matching between the additive printed graphene and the nickel current collector. Capacity retention over 98% can be maintained after 10000 cycles of charging and discharging. The composite electrodes show high capacitance as well as low inner resistance, without significant degradation when stacking up to 100 layers of 3D printing.

Experimental

Polyimide films (Kapton) of 200 μm thickness and nickel foams of 0.1 mm thickness were used directly after purchase. A DMG Lasertec 40 at 1064 nm with the CW mode

was used for the laser treatment. The output laser energy was set to 7 W with a writing speed of 800 mm/s. After printing, the multi-layer nickel foams (Figure S1) were pressed into thinner foams with 10 MPa pressure, as shown in Figure S2. A Tescan VEGA3 Scanning Electron Microscope (FESEM) with Energy Dispersive X-ray (EDX) spectroscopy was used for the morphology and elementary analysis. A Field Emission Electron TEM (JEOL Model JEM-2100F) was used for the high-resolution characterization. X-ray Photoemission Spectrometry (XPS) with a SKL-12 spectrometer, and an Mg Ka X-ray source was used for the characterizing the chemical elements. The Raman spectra was characterized with a LabRAM HR 800 Raman Spectrometer with a 488 nm laser source. The electrochemical measurement was performed using a Princeton VersaSTAT III electrochemical station. The CE8301 chips were used for the PWN step-up conversion. The input to output response of the step-up was measured using two Keithley 2450 SourceMeter SMU Instruments. The electrical conductivity was performed by four-point measurement using one Keithley 2450 SourceMeter SMU Instrument with potential-probe spacing at 7 cm.

For measuring the specific capacitance, the composite electrodes were cut into 1 cm by 1 cm in square shapes. The areal specific capacitance was calculated from GCD curves using the equation

$$C = \frac{I\Delta t}{s(\Delta V - IR)}$$

Where I is the constant discharge current, Δt is the discharging time, s is the area of the electrodes, ΔV is the potential range of the graphene/nickel electrode, and IR is the voltage drop due to the internal resistance.

Results and Discussions

The additive manufacturing processes of graphene/nickel composite electrodes are schematic illustrated in Figure 1. The crystalline structure of nickel is face center cubic phase with lattice constant of 0.352 nm, as shown in Figure 1a. Meanwhile, the lattice constant of the pristine monolayer graphene is 0.246 nm, as shown in Figure 1b. The structural parameter of the graphene can be extended up to 0.280 nm, when grown on the face (111) of nickel.[25] The catalytic mechanism of Ni (111) for graphene growth was also evidenced using DFT calculation and SPM characterization.[26] So if sufficient annealing (such as laser heating) is applied to graphene layers on nickel substrates, the crystalline lattices of graphene might match to the underlying nickel substrate, as denoted as AOC shape in Figure 1c, with stable electrochemical properties.[27-29]

In order to fabricate the graphene/nickel composites with high degree of lattice matching, a modified laser induced forward transfer process was introduced for additively depositing of graphene onto nickel foam substrate.[20] A flexible polyimide film is placed on a roll-to-roll holder for reeling and a pristine nickel foam is placed under the polyimide film. A laser beam spot at 1064 nm wavelength in the CW mode is focused onto the polyimide film, as shown in Figure 1d. Then the laser beam scribes the polyimide film along the computer designed patterns. The high temperature from the focused laser spot carbonizes the polyimide film into graphene membranes. When the laser energy is sufficiently large, the high temperature outgoing gases (such as CO_2) possess abundant kinetic energy to drive the graphene flakes towards the underlying nickel foam, as shown in Figure 1e. Thus, the synthesized graphene can be LIFT printed

onto the nickel current collector. Post laser scribing on the as-printed graphene provides an annealing effect for promoting the extended lattice structure of graphene according to the lattice structure of the nickel foam as well as a wetting surface for the graphene, as shown in Figure 1f.[22] For the second layer printing, another pristine nickel foam is placed onto the first layer. Then another LIFT printing of graphene and post laser treatment are applied to the second layer, as shown in Figure 1g and 1h, respectively. For continuously printing further layers, more pristine nickel foams are placed above the existing layers, followed by repeating the LIFT and post treatment processes, as shown in Figure 1i. Using this LIFT printing process, arbitrary shapes of LIFT printed graphene/nickel composite electrodes can be fabricated (as shown in Figure S3).

The morphologies of the LIFT printed composite electrodes were characterized with electron microscopy. The pristine nickel foam shows 3D microscale porous structures (Figure 2a), with relatively smooth surfaces (Figure 2b). After the LIFT printing, fuzzy flakes of graphene were seen above the porous nickel foam as in Figure 2c. The zoom-in observation of these additives reveals them as layered flakes, extending from nickel foam underneath, as shown in Figure 2d. After the post laser treatment, the fuzzy layers disappear, as shown in Figure 2e. Instead, a uniform coating of porous nanostructures was found on the 3D nickel foams as shown in Figure 2f. The nanostructures of the post treated graphene flakes were further examined with TEM as shown in Figure 2g. The crystalline lattices with ~0.35 nm d-spacing were clearly observed, indicating the polycrystalline nature of the graphene flakes. In addition, porous structures (highlighted in red) were randomly distributed among the graphene

flakes, as shown in Figure 2h, which benefit the access of electrolyte ions into these porous structures, which work as supercapacitor electrodes.

The chemical composition of the LIFT printed graphene was examined using spectra characterization. The Raman shift spectra of the samples in Figure 3a are featured with four prominent peaks. The G at 1580 cm^{-1} and 2D peak at 2700 cm^{-1} originating from second order zone-boundary phonons, and D peaks at 1350 cm^{-1} representing the sp^2-carbon bonds of both the as-printed and post-treated samples, indicated as typical few-layer graphene flakes with random orientation. Thus, the aromatic and imide repeat units in the polyimide are chemically reduced to graphene under such laser treatment. A slightly weaker peak in G for the as-printed electrodes indicates a higher defect ratio than the post-treated sample. To verify such differences, XPS analysis was also performed on both samples. As shown in Figure 3b, the as-prepared sample contains 90% carbon, while the oxygen and nitrogen peaks are still recognizable. Further, the post-laser treated sample showed higher carbon, less nitrogen and no oxygen signals (Figure 3c). Hence, it can be inferred that the high temperature during the post laser treatment can further break the remaining C-O, C=O and N-C bonds, so that more graphene ratios remain. These spectral changes indicate that post treatment can further increase the graphene ratios within the composites.

To study the performance of supercapacitors with the LIFT printed electrodes, symmetrical electrodes in 1 M KOH aqueous electrolytes were assembled, as shown in Figure S4. The CV curves of different layers of printing are shown in Figure 4a with layer numbers ranging from 1 to 10. The quasi-rectangular shape of the CV curve

proves the dominance of the EDLC mechanism. The increased number of layers did not compromise the EDLC performance, demonstrating its high scalability for 3D printing of thicker electrodes. To examine the charger transfer within the graphene/nickel electrodes with different layer numbers of 3D printing, classical electrochemical impedance spectroscopy is used with frequency ranging from 100 kHz to 0.01 Hz. The Nyquist plot of the device in Figure 4b shows that all their equivalent series resistances (ESR) are small, suggesting that their high conductivities (359,712 S/m) are preserved even with 10 layers of printing. The connecting resistance between the graphene flakes and the nickel collectors were low, as suggested by the small ESR values ranging from 0.78 to 1.06 Ω as shown in Figure S5a-d. The charge transfer resistance R_{ct} and the double layer capacitance C_d are represented by the semicircular diameter of the Nyquist curve at the high frequency zone. Short diffusion distances can be deduced according to the smaller semicircular diameters as the layers of printing increased. For the 10 layers of 3D printed electrode, the R_{ct} is as low as 0.14 Ω, indicating the ultra-low inner resistance of the active graphene materials. At low frequencies, ideal capacitive behaviors were observed for all different layers, with a nearly vertical plot with frequency lower than 1 Hz.

The GCD plots of the devices show a linear charging and discharging curve, further proving their effective EDLC storage mechanisms, as shown in Figure 4c. The specific capacitance of these 3D printed supercapacitor devices was calculated from the GCD plots using the equation $C=I \cdot t/V$, and plotted according to the different current densities in Figure 4d. With the layer number increased from 1 to 100, the specific capacitance

of these supercapacitor devices increased from 10 to 995 mF/cm^2 (~27.47 mF/cm^2 in the three-electrode configuration in Figure S6 at 50 mV/s), indicating its outstanding scalability for additive manufacturing. The areal capacitance of this composite electrode is significantly larger than traditional techniques for EDLC supercapacitors, and even 6 times larger than the original laser induced graphene.[9, 30, 31] The areal normalized Ragone plot show increased performance in terms of areal energy and power density as the layer of 3D printing increased, as shown in Figure 4e. Highest device power density at 9.39 mW/cm^2 was achieved at 55.9 μW/cm^2 energy density with 100 layers of LIFT 3D printing. And even with one layer printed electrode, the performance was significantly enhanced compared to the reported LIG synthesized with directly CO_2 laser.[32] The robust retention greater than 98% is shown in Figure 4f, with quasi-linear charging and discharging slops at 10,000 cycles. The self-discharge curves for the 3D printed electrode shows two significant effects as in Figure S7. Although a relatively quick 0.2 V voltage drop was observed in the first 10 minutes, the following voltage drop became much slower with another 0.2 V drop for the additional 50 minutes.

The electrical energy storage mechanism determines that the supercapacitor cannot provide a constant output voltage. Unlike batteries with fixed voltage windows defined by the redox reaction, the attaching and detaching of ions at the electrode/electrolyte interface is not able to maintain a constant electrical potential for the supercapacitor. Although pseudocapacitance can provide a similar flat stage within a certain voltage range, it cannot meet the requirement for practical use as a powering source.[33] Usually,

a DC-DC converter is recommended for using supercapacitors to power the actual devices.[34] In principle, there are two types of DC-DC converters, step-down and step-up ones. The step-down type DC-DC simply reduces the input potential from the supercapacitor down to a lower potential, providing a constant output voltage. However, when the output voltage of the supercapacitor is below the required voltage of the electrical appliance, the electrical loads cannot receive sufficient energy to work functionally. Recently, the development of the step-up DC-DC converter is booming, thanks to the progress in semiconductor technologies. Using pulse-width modulation (PWM) generators, lower input voltages can be raised to higher output voltages.[35] Since the voltages of supercapacitors always decrease during discharge, we find these PWM generators very useful for powering electrical appliances at higher voltage from lower voltage supercapacitors.

The application of such a supercapacitor as a 5 V output voltage powering source is demonstrated using a USB adaptor combined with a PWM type step-up DC-DC converter. The anode and cathode of the punch cell type supercapacitor are connected to the positive and negative pins of the DC-DC converter circuits, respectively, as shown in Figure 5a. The PWM block on the circuits can constantly provide an output the voltage at 5 V to the USB adaptor, using the circuit shown in Figure S8. When the supercapacitor is discharging, the left and the right pin of the USB adaptor can supply 5 V DC voltage, like commercial chargers, as shown in Figure 5b. The actual output voltage of the in-series supercapacitor was monitored using a USB power meter, as shown in Figure 5c. Although the voltage of the supercapacitor would decrease

according to the GCD plots in Figure 4c, the output voltage of the USB adaptor can be maintained at around 5 V until 80% of the capacitance (from 5V to 1V) is drained, thanks to the circuitry. The actual USB voltages according to different supercapacitor output voltages are plotted in Figure 5d. For the five in-series supercapacitors with output voltage ranging from 5 V to 1 V, the actual USB voltage fluctuates between 5.25 V to 4.98 V, which is below a 5% variation. So these 3D printed supercapacitors can successfully serve as powering sources for 5 V USB charging, with over 80% efficiency.

Supercapacitors combine the advantages of both batteries and capacitors, with adequate charging rates and capacity. Although they have huge potential for powering a wide range of devices, the reported literatures on supercapacitor research barely explores their constant-voltage powering functions. For example, most papers only mention their applications for powering up an LED, a lamp, or charging a phone for a very short duration. Although over two billion smartphones are used every day, unfortunately, very few studies have addressed the potential of using supercapacitors for the USB charging devices.[36]

In this research, we successfully 3D printed graphene/nickel supercapacitor electrodes with high scalability, high capacitance and low resistance. Compared to the existing literature on EDLC supercapacitors, our current research provides advances in several aspects. Even though a pure graphene composite can demonstrate even larger volume capacitance, the relatively large overall resistance would decrease the performance when scaling up.[37] The CVD growth of graphene on metal current collectors can have even higher conductivity than in our study, however, the time and

costs in CVD is higher larger than laser scribing at ambient conditions.[18] Although hydrothermal methods can also deposit carbon materials onto metal current collectors, these labor-intensive procedures are not so straightforward compared to robotic fabrication processes.[38] Although the existing LIGs on polyimide films can work as microsupercapacitor, as illustrated in Figure S9, their relatively low conductivities (92 S/m calculated with our four-probe measurement) limit their direct application as large capacity powering sources. The direct contact of graphene on the nickel current collector decreases the inner resistance of the electrode, so the performance of the supercapacitor can be sustained when stacking in higher performance devices.[39]

Although this research has addressed several issues related to the application of supercapacitors for 5V USB charging, some improvements can still be made on the current research. Even though graphene can provide high capacitance, however, the EDLC mechanism still stores less energy than the pseudocapacitive supercapacitors. The actual lattice matching between the 3D printed graphene on the nickel surfaces are still not know. A more detailed study on a thinner layer of graphene on the single crystalline Ni (111) surface should be carried to investigate its inner mechanism for such stable composite electrodes. Adding pseudocapacitive additives onto the existing 3D printed graphene/nickel electrodes might further enhance the capacitance of the supercapacitors.[33, 40] The scope of current research was limited to the aqueous electrolyte-based supercapacitor. The graphene might not fully cover the inner structures of the nickel foam surfaces, and specific consideration should be given for the selection of electrolyte, preventing the potential etching of electrolyte on the

exposed nickel surfaces. The application of a state-of-the-art organic electrolyte might further boost the performance of such capacitors.[13] The laser parameters also play important roles on the influence of surface pore structures of the laser induced graphene. To correlate the specific capacitance and the rate performance of composited electrodes on these pore structure, a more systemically study will be carried out according to different laser writing speeds and powers in the future.

Conclusions

In summary, we have demonstrated a novel type of LIFT printed 3D supercapacitor electrodes with high degree of lattice matching between the functional graphene flakes and the nickel current collectors. These highly-scalable graphene/nickel composite electrode with optimized porosity can achieve high performance for practical supercapacitor applications. Their high electrical conductivity, stability, and specific capacitance provide robust performances as supercapacitor electrodes. The high efficiency PWM step-up converter demonstrate great potential for outstanding performance supercapacitors as portable powering sources with constant output voltages. We anticipate the development of supercapacitors will benefit the end users of future portable devices, as fast charging powering sources.

Acknowledgements

The project was funded by the Postdoctoral Fellowship Scheme of the Hong Kong Polytechnic University with project number G-YW2R.

Conflict of Interest

The authors declare no conflict of interest.

Keywords: 3D printing, supercapacitor, graphene, USB, laser induced forward transfer

Figures

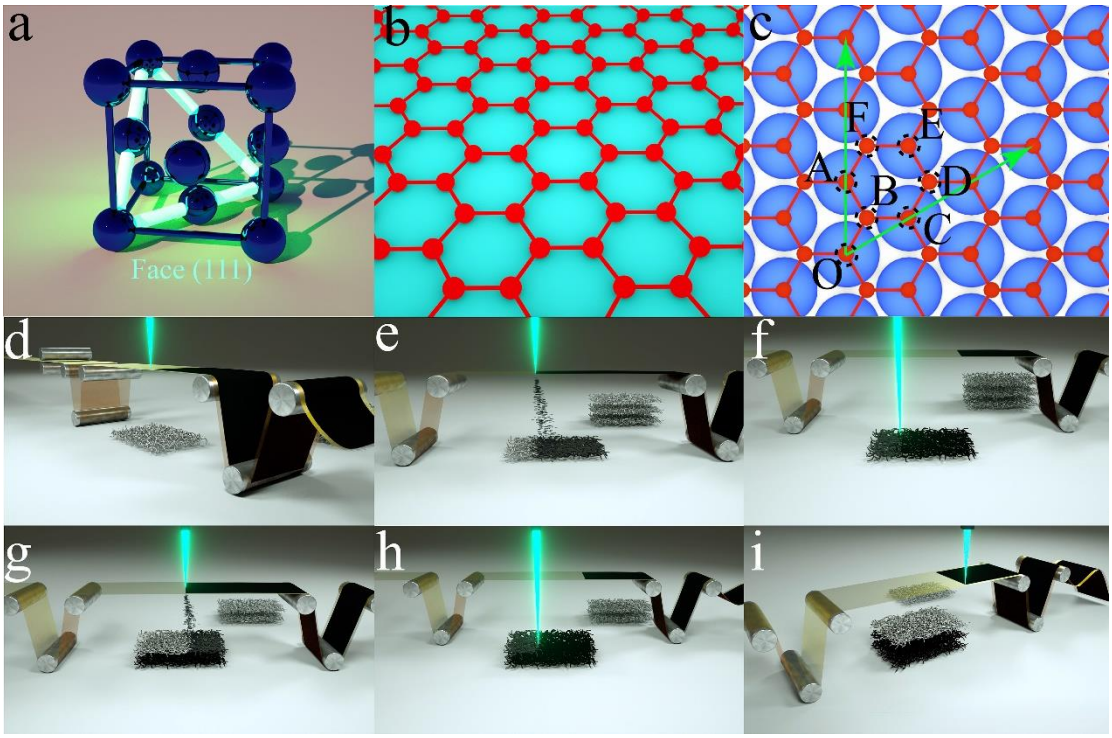

Figure 1. Schematic illustration of the LIFT printing process for fabricating the graphene/nickel electrodes. (a) The crystalline structure of face center cubic phase nickel, with the face (111) highlighted. (b) The molecule structure of mono layer graphene. (c) The lattice matching of the Basel plane graphene onto face (111) of nickel. (d) A pristine nickel foam is placed below the polyimide as the first layer. (e) Initial deposition of graphene onto the nickel foam becomes the first layer. (f) Post laser treatment of the first graphene layer ensures its firm contact to the nickel foam. (g) The second scribing deposits the graphene onto the second layer nickel foam. (h) A laser scribing post treats the second layers of graphene. (i) For printing more layers, similar steps will be repeated.

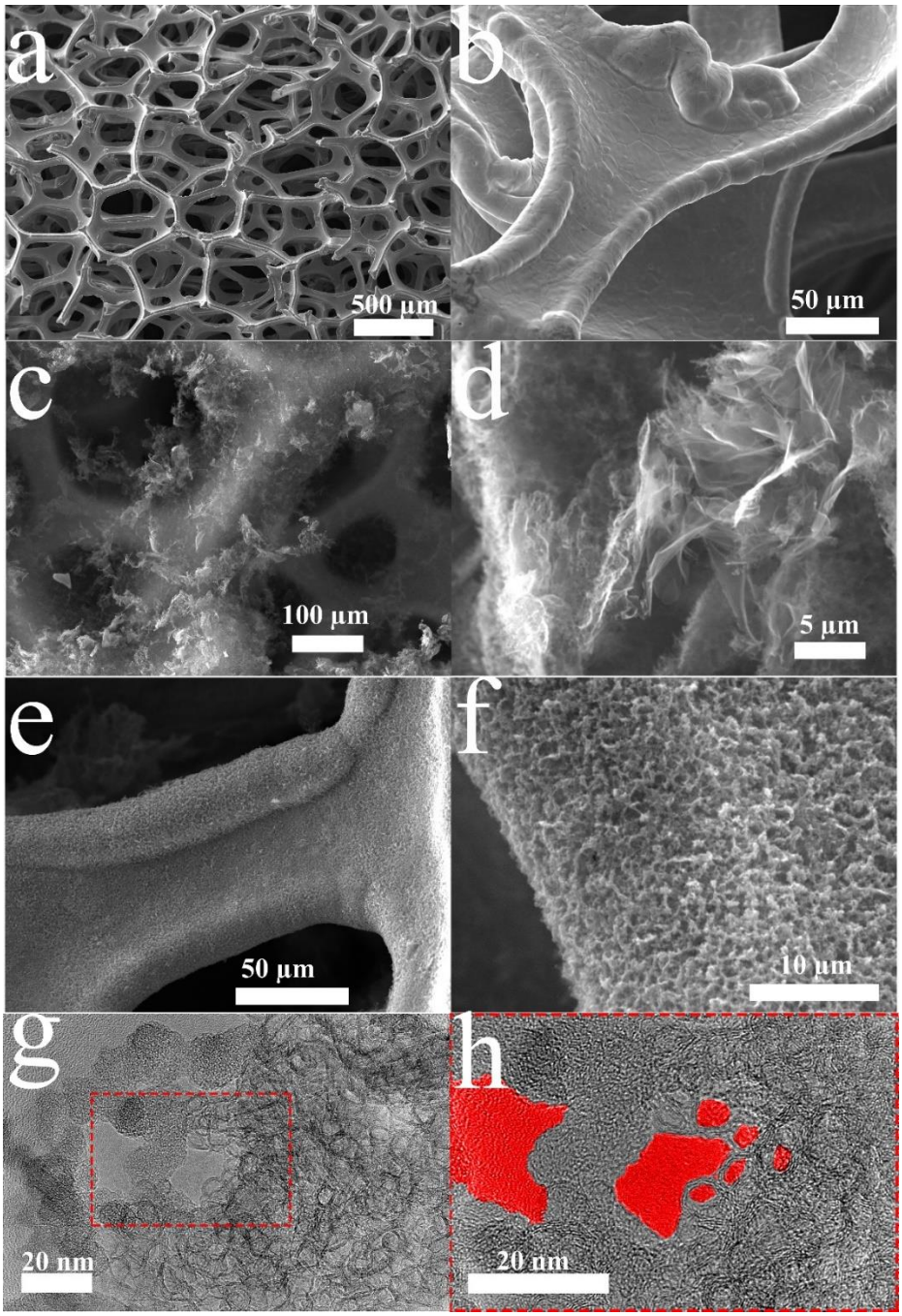

Figure 2. Electron microscopy images of the LIFT printed electrodes. SEM images of the pristine nickel form show a smooth surface in zoom-out (a) and zoom-in (b) view. As-printed graphene flakes distribute on the nickel foam in zoom-out (c) and zoom-in (d) view. Post treated graphene distribute randomly on the nick foam in zoom-out (e) and zoom-in (f) view. TEM images of the treated graphene (g) and its magnification view (h).

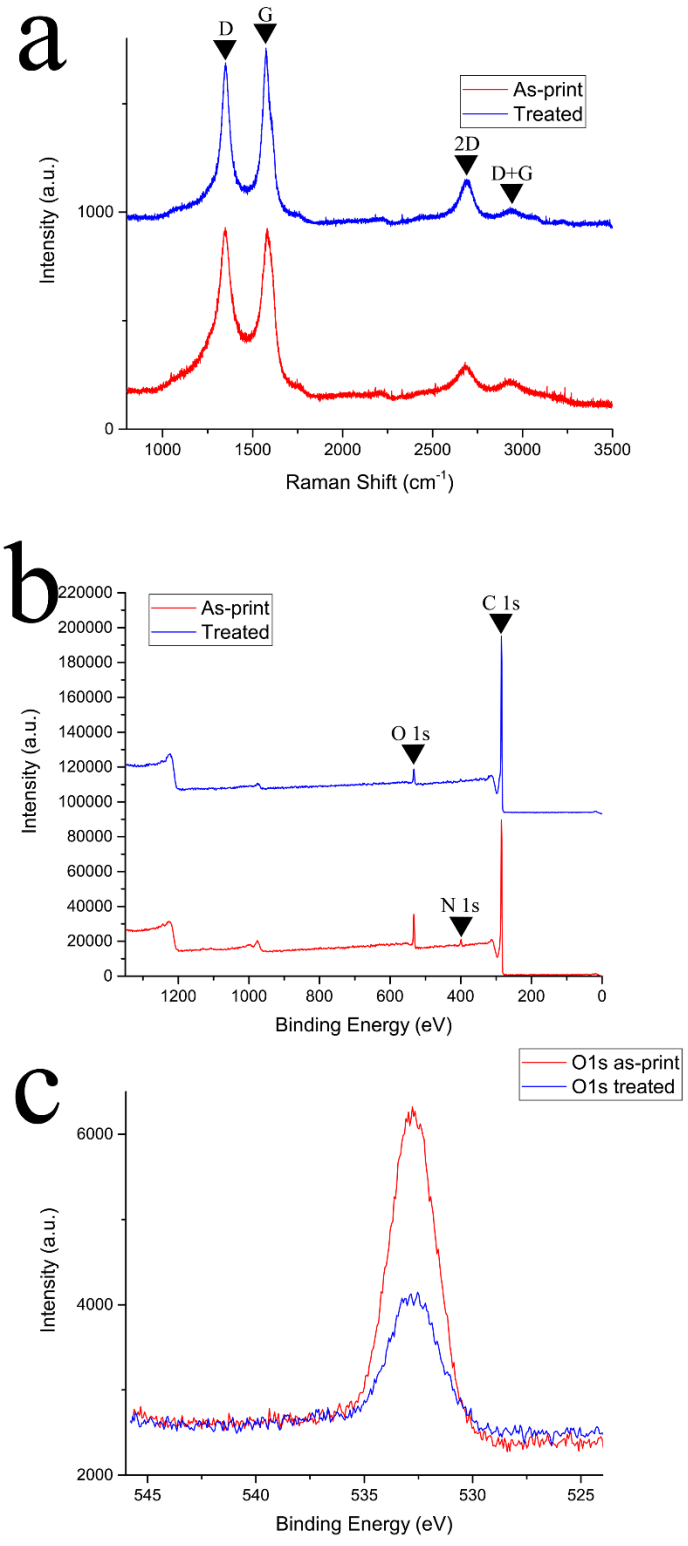

Figure 3. Spectra analysis of the LIFT printed graphene. (a) Raman spectra of the as-printed and treated graphene. (b) XPS spectra of the as-printed and treated graphene. (c) XPS O1s spectra of the as-printed and treated graphene.

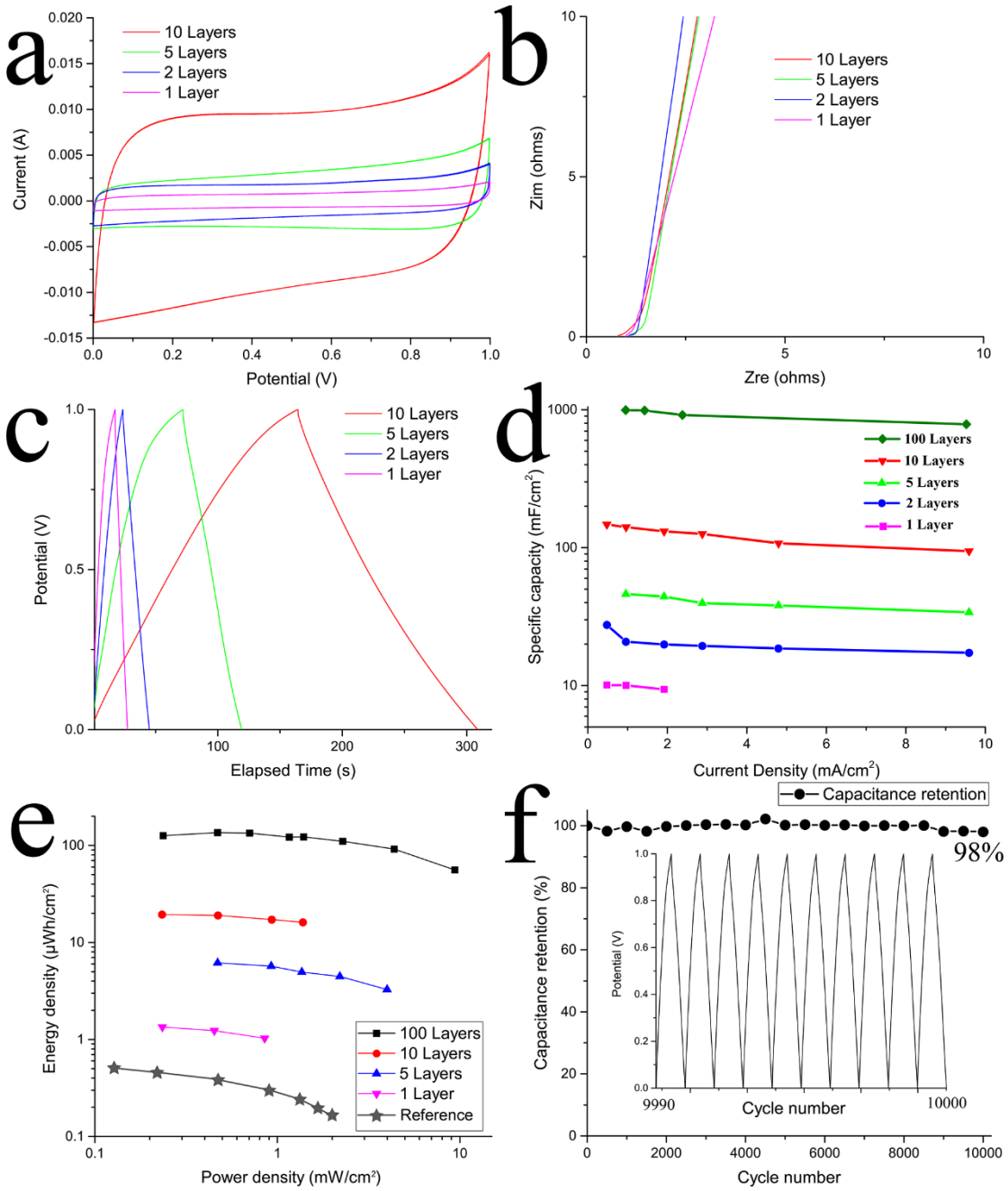

Figure 4. Electrochemical characterization of the assembled 3D printed supercapacitor devices. (a) The measured cyclic voltammetry curves of the LIFT printed graphene/nickel electrodes, with different layers of 3D printing. (b) The EIS slop of the LIFT printed graphene/nickel electrodes, with different layers of 3D printing. (c) The galvanostatic charge/discharge curves of the LIFT printed graphene/nickel electrodes at 1 mA/cm^2, with different layers of 3D printing. (d) Comparison of specific

capacitances with different layers of LIFT printed graphene/nickel electrodes. (e) Ragone plot of the areal energy and power densities of the LIFT printed supercapacitor with different layers of number, compared to the reference[32]. (f) Capacitance retention under repeated cycling at a current density of 1 mA/cm^2 for 10,000 cycles and the corresponding GCD plots at 10,000 cycles (inset).

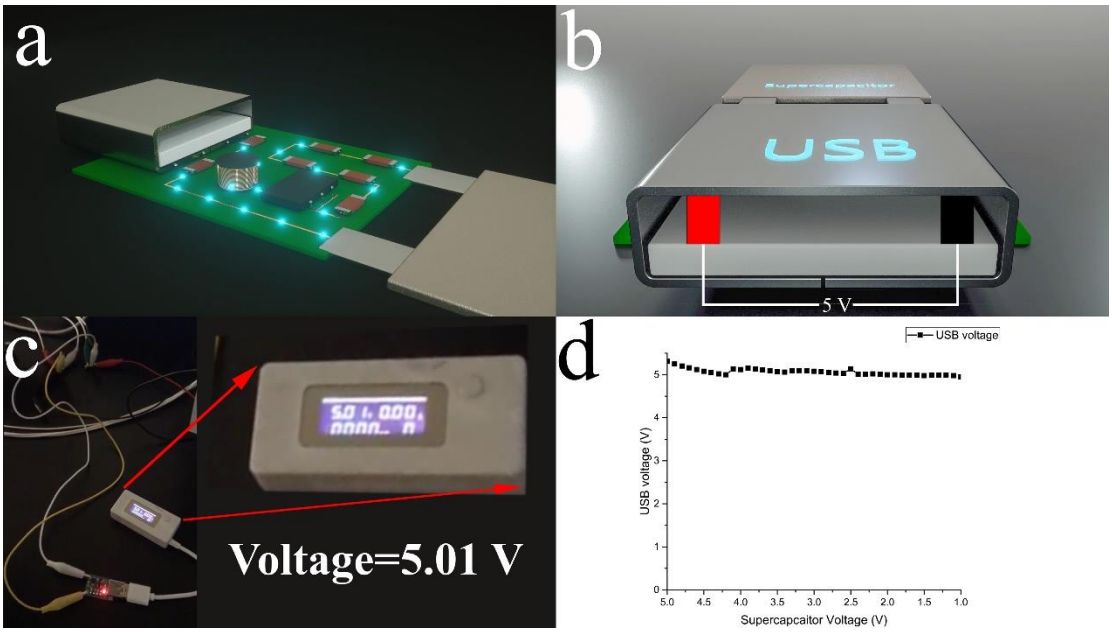

Figure 5 A supercapacitor connected with a DC-DC converter. The frontal (a) and side view (b) schematic illustration of the PWM DC-DC converter with a supercapacitor and USB connector. (c) The photo of a USB multimeter measuring the output voltage of supercapacitor powered USB charger. (d) The relationship of USB output voltage according to different input voltages from the supercapacitor.

Reference

1. P. Huang, C. Lethien, S. Pinaud, K. Brousse, R. Laloo, V. Turq, M. Respaud, A. Demortiere, B. Daffos, P. L. Taberna, B. Chaudret, Y. Gogotsi and P. Simon, *Science*, 2016, **351**, 691-695.
2. P. Simon, Y. Gogotsi and B. Dunn, *Science*, 2014, **343**, 1210-1211.
3. D. Sheberla, J. C. Bachman, J. S. Elias, C. J. Sun, Y. Shao-Horn and M. Dinca, *Nat. Mater.*, 2017, **16**, 220-224.
4. S. X. Zuo, J. Chen, W. J. Liu, X. Z. Li, Y. Kong, C. Yao and Y. S. Fu, *Carbon*, 2018, **129**, 199-206.
5. L. J. Yang, D. Li, T. T. Yan, G. R. Chen, L. Y. Shi, Z. X. An and D. S. Zhang, *ACS Appl. Mater. Interfaces*, 2018, **10**, 42494-42502.
6. L. J. Yan, D. Li, T. T. Yan, G. R. Chen, L. Y. Shi, Z. X. An and D. S. Zhang, *ACS Sustainable Chemistry & Engineering*, 2018, **6**, 5265-5272.
7. H. Y. Duan, T. T. Yan, G. R. Chen, J. P. Zhang, L. Y. Shi and D. S. Zhang, *Chem. Commun. (Camb.)*, 2017, **53**, 7465-7468.
8. R. Ye, D. K. James and J. M. Tour, *Acc. Chem. Res.*, 2018, DOI: 10.1021/acs.accounts.8b00084.
9. J. Lin, Z. W. Peng, Y. Y. Liu, F. Ruiz-Zepeda, R. Q. Ye, E. L. G. Samuel, M. J. Yacaman, B. I. Yakobson and J. M. Tour, *Nat. Commun.*, 2014, **5**, 5714.
10. P. L. Taberna, C. Portet and P. Simon, *Applied Physics a-Materials Science & Processing*, 2006, **82**, 639-646.

11. D. Pech, M. Brunet, H. Durou, P. H. Huang, V. Mochalin, Y. Gogotsi, P. L. Taberna and P. Simon, *Nat. Nanotechnol.*, 2010, **5**, 651-654.

12. J. Chmiola, C. Largeot, P. L. Taberna, P. Simon and Y. Gogotsi, *Science*, 2010, **328**, 480-483.

13. E. Mourad, L. Coustan, P. Lannelongue, D. Zigah, A. Mehdi, A. Vioux, S. A. Freunberger, F. Favier and O. Fontaine, *Nat. Mater.*, 2017, **16**, 446-454.

14. K. Marcus, K. Liang, W. Niu and Y. Yang, *The Journal of Physical Chemistry Letters*, 2018, **9**, 2746-2750.

15. K. Liang, K. Marcus, Z. Z. Yang, L. Zhou, H. Pan, Y. L. Bai, Y. G. Du, M. H. Engelhard and Y. Yang, *Small*, 2018, **14**.

16. K. Liang, L. Ju, S. Koul, A. Kushima and Y. Yang, *Adv. Energy Mater.*, 2018, **0**, 1802543.

17. K. Liang, K. Marcus, S. Zhang, L. Zhou, Y. Li, S. T. De Oliveira, N. Orlovskaya, Y.-H. Sohn and Y. Yang, *Adv. Energy Mater.*, 2017, **7**, 1701309.

18. J. R. Miller, R. A. Outlaw and B. C. Holloway, *Science*, 2010, **329**, 1637-1639.

19. C. W. Visser, R. Pohl, C. Sun, G. W. Roemer, B. H. in 't Veld and D. Lohse, *Adv. Mater.*, 2015, **27**, 4087-4092.

20. W. K. C. Yung, B. Sun, Z. Meng, J. Huang, Y. Jin, H. S. Choy, Z. Cai, G. Li, C. L. Ho, J. Yang and W. Y. Wong, *Sci. Rep.*, 2016, **6**, 39584.

21. G. Li, W.-C. Law and K. C. Chan, *Green Chem.*, 2018, **20**, 3689-3695.

22. G. Li, X. Mo, W.-C. Law and K. C. Chan, *ACS Appl. Mater. Interfaces*, 2018, DOI: 10.1021/acsami.8b17419.

23. W. K. C. Yung, B. Sun, J. Huang, Y. Jin, Z. Meng, H. S. Choy, Z. Cai, G. Li, C. L. Ho, J. Yang and W. Y. Wong, *Sci. Rep.*, 2016, **6**, 31188.

24. W. K. C. Yung, G. Li, H. M. Liem, H. S. Choy and Z. Cai, *J. Mater. Chem. C*, 2015, **3**, 11294-11299.

25. R. Rosei, M. Decrescenzi, F. Sette, C. Quaresima, A. Savoia and P. Perfetti, *Physical Review B*, 1983, **28**, 1161-1164.

26. L. L. Patera, F. Bianchini, C. Africh, C. Dri, G. Soldano, M. M. Mariscal, M. Peressi and G. Comelli, *Science*, 2018, **359**, 1243-1246.

27. G. J. Li, C. W. Leung, Y. C. Chen, J. H. Hsu, A. C. Sun, K. W. Lin and P. W. T. Pong, *IEEE Trans. Magn.*, 2013, **49**, 3310-3313.

28. G. Li, C. W. Leung, Y.-C. Chen, K.-W. Lin, A.-C. Sun, J.-H. Hsu and P. W. T. Pong, *Microelectron. Eng.*, 2013, **110**, 241-245.

29. G. J. Li, C. W. Leung, Z. Q. Lei, K. W. Lin, P. T. Lai and P. W. T. Pong, *Thin Solid Films*, 2011, **519**, 8307-8311.

30. W. J. Hyun, E. B. Secor, C. H. Kim, M. C. Hersam, L. F. Francis and C. D. Frisbie, *Adv. Energy Mater.*, 2017, **7**.

31. L. Wen, F. Li and H. M. Cheng, *Adv. Mater.*, 2016, **28**, 4306-4337.

32. Y. L. Li, D. X. Luong, J. B. Zhang, Y. R. Tarkunde, C. Kittrell, F. Sargunaraj, Y. S. Ji, C. J. Arnusch and J. M. Tour, *Adv. Mater.*, 2017, **29**, 1700496.

33. H. G. Zhang, X. D. Yu and P. V. Braun, *Nat. Nanotechnol.*, 2011, **6**, 277-281.

34. N. A. Kyeremateng, T. Brousse and D. Pech, *Nat. Nanotechnol.*, 2017, **12**, 7-15.

35. B. J. Byen, C. H. Ban, Y. B. Lim and G. H. Choe, *Journal of Power Electronics*,

2017, **17**, 1413-1421.

36. S. The Statistics Portal, Number of Mobile Phone Users Worldwide from 2015 to 2020, www.statista.com/statistics/274774/forecast-of-mobile-phone-users-worldwide/, 9 Jul 2018).

37. W. Gao, N. Singh, L. Song, Z. Liu, A. L. M. Reddy, L. J. Ci, R. Vajtai, Q. Zhang, B. Q. Wei and P. M. Ajayan, *Nat. Nanotechnol.*, 2011, **6**, 496-500.

38. D. S. Yu, K. Goh, H. Wang, L. Wei, W. C. Jiang, Q. Zhang, L. M. Dai and Y. Chen, *Nat. Nanotechnol.*, 2014, **9**, 555-562.

39. Z. W. Peng, J. Lin, R. Q. Ye, E. L. G. Samuel and J. M. Tour, *ACS Appl. Mater. Interfaces*, 2015, **7**, 3414-3419.

40. P. Simon and Y. Gogotsi, *Nat. Mater.*, 2008, **7**, 845-854.